Neurobiology of Disease 127 (2019) 449–461

Contents lists available at ScienceDirect

Neurobiology of Disease

journal homepage: www.elsevier.com/locate/ynbdi

Reciprocal modulation between amyloid precursor protein and synaptic membrane cholesterol revealed by live cell imaging

Claire E. DelBove[a], Claire E. Strothman[b], Roman M. Lazarenko[a], Hui Huang[c], Charles R. Sanders[c,d], Qi Zhang[a,e,*]

[a] Department of Pharmacology, Vanderbilt University, United States of America
[b] Department of Cell and Developmental Biology, Vanderbilt University, United States of America
[c] Department of Biochemistry, Vanderbilt University, United States of America
[d] Department of Medicine, Vanderbilt University Medical Center, United States of America
[e] Brain Institute, Florida Atlantic University, United States of America

ARTICLE INFO

Keywords:
Amyloid precursor protein
Trafficking
Proteolysis
Membrane
Cholesterol
Synapse

ABSTRACT

The amyloid precursor protein (APP) has been extensively studied because of its association with Alzheimer's disease (AD). However, APP distribution across different subcellular membrane compartments and its function in neurons remains unclear. We generated an APP fusion protein with a pH-sensitive green fluorescent protein at its ectodomain and a pH-insensitive blue fluorescent protein at its cytosolic domain and used it to measure APP's distribution, subcellular trafficking, and cleavage in live neurons. This reporter, closely resembling endogenous APP, revealed only a limited correlation between synaptic activities and APP trafficking. However, the synaptic surface fraction of APP was increased by a reduction in membrane cholesterol levels, a phenomenon that involves APP's cholesterol-binding motif. Mutations at or near binding sites not only reduced both the surface fraction of APP and membrane cholesterol levels in a dominant negative manner, but also increased synaptic vulnerability to moderate membrane cholesterol reduction. Our results reveal reciprocal modulation of APP and membrane cholesterol levels at synaptic boutons.

1. Introduction

Amyloid plaques, one of the pathohistological hallmarks of Alzheimer's disease (AD), are primarily comprised of β-amyloid peptides (Aβs). Aβs are proteolytic products of the amyloid precursor protein (APP), an integral membrane protein with a single transmembrane domain (Kang et al., 1987; Reinhard et al., 2005). Due to its linkage to AD, APP and its proteolytic processing have been investigated extensively since the early 1990s (Hardy and Allsop, 1991). It has been well demonstrated that APP is subject to two routes of proteolytic processing, amyloidogenic and nonamyloidogenic, catalyzed by three proteases known as the α-, β- and γ-secretases (αS, βS and γS) (Fig. 1A) (Haass et al., 2012). In the amyloidogenic pathway, APP is first cleaved by βS in its membrane-proximal ectodomain to generate a large soluble peptide (sAPPβ) and a membrane-bound C-terminal fragment (CTF or specifically C99 for its 99 amino acid residues). Subsequently, C99 is cleaved by γS within the transmembrane domain, yielding Aβs and a short intracellular C-terminal fragment (AICD). In the nonamyloidogenic pathway, APP is first cleaved by αS in the middle of Aβ sequence, yielding a longer soluble ectodomain (sAPPα) and a membrane-bound 83-residue CTF (C83). C83 is also cleaved by γS within the transmembrane domain, generating a shorter 30-residue peptide (P3) and an identical AICD (Haass et al., 1992).

Many early studies on APP processing have been conducted in non-neuronal cells (Chen et al., 2015; Sun and Roy, 2017) for technical practicality. They showed that the majority of the APP was located in the intracellular membranes of the Golgi and trans-Golgi network (TGN) and a small portion was sorted to the plasma membrane (Kuentzel et al., 1993). αS cleaves APP in the plasma membrane and βS cleaves APP in endocytic compartments (Parvathy et al., 1999; Refolo et al., 1995), suggesting that APP's subcellular membrane localization determines its non-amyloidogenic or amyloidogenic fate. Notably, the plasma membrane generally has more cholesterol than most intracellular membranes (> 13 mol% vs. ~5 mol% of total membrane lipids) (van Meer et al., 2008), and cholesterol upregulates the proteolytic activities of βS (von Arnim et al., 2008; Xiong et al., 2008) and γS (Grimm et al., 2008; Runz et al., 2002; Xiong et al., 2008) but suppresses αS (Bodovitz and Klein, 1996; Kojro et al., 2001).

* Corresponding author at: Brain Institute, Florida Atlantic University, 5353 Parkside Dr., Rm 101, MC-17, Jupiter, FL 33458, United States of America.
E-mail address: zhangq@health.fau.edu (Q. Zhang).

https://doi.org/10.1016/j.nbd.2019.03.009
Received 8 October 2018; Received in revised form 3 February 2019; Accepted 12 March 2019
Available online 15 March 2019
0969-9961/

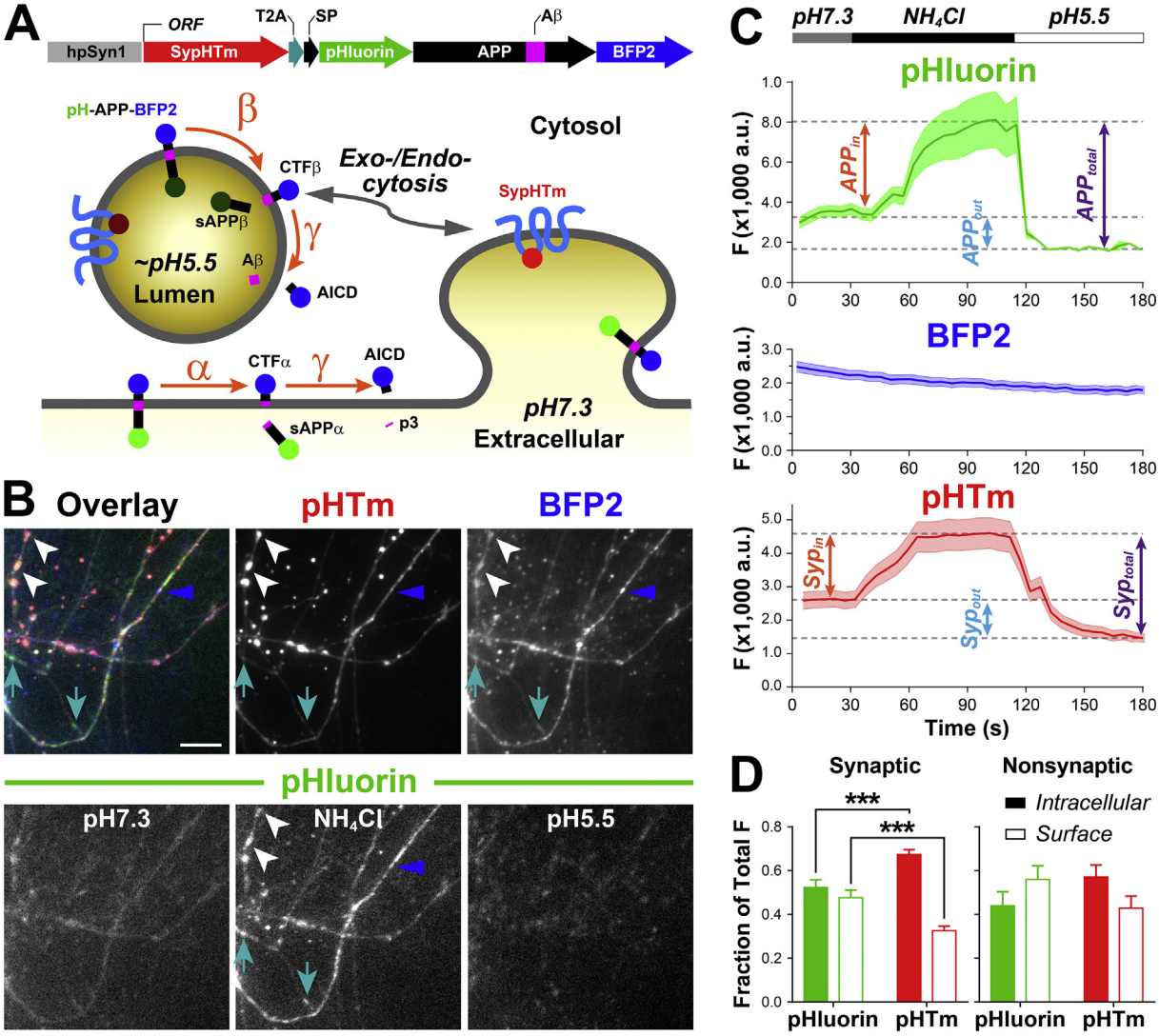

Fig. 1. SypHTm:T2A:pH-APP-BFP2 reports APP distribution and marks synaptic vesicles.
A, the upper diagram illustrates the transgene construct including human Synapsin I promoter (hpSyn1) and an open reading frame (ORF) comprised of Synaptophysin-pHTomato (SypHTm), *thosea asigna* virus 2A peptide (T2A), APP signal peptide (SP), pHluorin (pH), APP including the Aβ region, and blue fluorescence protein 2 (BFP2). The cartoon demonstrates how extracellular pH and exo−/endocytosis affect pHluorin and pHTm fluorescence (dark (i.e. quenched) vs. bright (i.e. unquenched) green or red dots at pH 5.5 vs. 7.3, respectively) and how the α-, β-, and γ-secretases (α, β, and γ in the cartoon) cleave pH-APP-BFP2. In acidic intracellular compartments such as endosomes and synaptic vesicles, pHluorin and pHTm are quenched and pH-dependent β-cleavage occurs, producing Aβ. AICD, APP intracellular domain; CTFα/β, APP's C-terminal fragment after α- or β-secretase cleavage; P3, P3 peptide generated by α- and γ-secretase cleavage. B, top left, overlay of SypHTm (red), pHluorin (green) in 50 mM NH_4Cl, and BFP2 (blue); top middle, SypHTm in 50 mM NH_4Cl; top right, averaged BFP2 throughout the course of the experiment; bottom: pHluorin in normal Tyrode's solution (pH 7.3), in 50 mM NH_4Cl and in pH 5.5 Tyrode's solution. White arrowheads indicate synaptically co-localized SypHTm and pH-APP-BFP2, cyan arrows indicate non-synaptic pH-APP-BFP2, and the blue arrowheads indicate nonsynaptic CTF because of strong BFP2 and weak pHluorin signals. Scale bar, 10 μm. C, example of continuous changes of pHluorin, BFP2 and pHTm fluorescence in one FOV (field of view) containing 39 ROIs (regions of interest) during sequential applications of pH 7.3 Tyrode's solution, 50 mM NH_4Cl, and pH 5.5 Tyrode's solution. Double-ended arrows indicate the calculations of surface, intracellular and total APP and Syp based on fluorescence intensity differences. Shadows are SEM. D, quantification of the fraction of total pHluorin (green) and pHTm (red) fluorescence located intracellularly (solid bars) and at the cell surface (open bars) in the synapses (left) and nonsynaptic areas (right). From left to right, the mean ± SEM of these subcellular fractions is pHluorin(in)/Total = 0.524 ± 0.035, pHluorin(out)/Total = 0.476 ± 0.035, pHTm(in)/Total = 0.674 ± 0.021 and pHTm(out)/Total = 0.326 ± 0.021 in the synapses, and pHluorin(in)/Total = 0.441 ± 0.063, pHluorin(out)/Total = 0.559 ± 0.063, pHTm(in)/Total = 0.571 ± 0.055, pHTm(out)/Total = 0.429 ± 0.055 in nonsynaptic regions. There was a significant difference between pHluorin and pHluorin regarding surface or intracellular fractions according to a two-tailed paired *t*-test (***, $p = .001$). No significant difference was found for the nonsynaptic ROIs (two-tailed paired t-test, $p = .0543$). Synaptic ROIs, $n = 47$; nonsynaptic ROIs, $n = 23$. Error bars represent SEM. (For interpretation of the references to colour in this figure legend, the reader is referred to the web version of this article.)

Neurons are morphologically unique for their polarity, extended neurites, and intercellular connections known as synapses. Accordingly, they have higher surface area and more complicated cellular membrane system than non-neuronal cells do. The distinct lipid composition of the neuronal surface membrane, especially its high cholesterol content and its electrophysiological properties, has profound influence on membrane proteins like APP. APP is enriched at the presynaptic terminals (a.k.a. synaptic boutons) including synaptic vesicles (SVs) (Groemer et al., 2011; Wilhelm et al., 2014). Its expression, distribution, and cleavage are reportedly influenced by neuronal activity (Dawkins and Small, 2014). Moreover, its proteolytic products are believed to reciprocally modulate neuronal activity (Cirrito et al., 2008; Wang et al., 2017). Reportedly, the three secretases also regulate synaptic transmission and plasticity (Wang et al., 2012). Interest in neuronal APP has

recently surged due to heated debate about the amyloid hypothesis (Herrup, 2015; Makin, 2018; Musiek and Holtzman, 2015) and findings about neuron-specific mechanisms of APP (Das et al., 2013; Das et al., 2016; Sun and Roy, 2017).

Owing to its spatiotemporal resolution, live-cell fluorescence imaging is well suited for studying synaptic changes in morphologically complex neurons. New fluorescent reporters enable the use of live-cell imaging to qualitatively and quantitatively measure subcellular APP distribution. For example, by labeling APP and BACE-1 with two different fluorescent proteins and with two complementary parts of one fluorescent protein, Das et al revealed activity-dependent and independent convergence of these two proteins in different intracellular compartments (Das et al., 2013; Das et al., 2016) that could not be observed in non-neuronal cells. Groemer et al tagged APP's N-terminal with a pH-sensitive green fluorescence protein (i.e. pHluorin) and quantified the coupling between APP trafficking and SV turnover for the first time (Groemer et al., 2011).

APP trafficking and processing in subcellular membranes of live neurons is important to APP's physiological and pathological roles. Therefore, we decided to investigate factors regulating APP using a multi-fluorescence reporter and live cell imaging. We generated pH-APP-BFP2 by adding a pH-insensitive BFP2 at pH-APP's C-terminal, and co-expressed a pH-sensitive red fluorescence reporter selective for SVs (Synaptophysin-pHTomato, SypHTm) (Li and Tsien, 2012) via a bicistronic construct. We performed multichannel live cell imaging to investigate the effects of neuronal activity and cholesterol on APP's subcellular distribution and trafficking. Our results not only shed light on APP surface turnover but also revealed a direct inverse correlation between surface membrane cholesterol and APP, especially at synaptic boutons.

2. Results

2.1. Construction and characterization of a triple-fluorescence reporter system

We built our reporter on Groemer's pH-APP construct (gifted by J. Klingauf). The pH-APP expression is driven by a human Synapsin 1 promoter (hpSynI) to ensure neuron-specific and moderate expression (Kügler et al., 2001). It is based on rat APP695, which matches the endogenous APP predominantly expressed by neurons in our rat postnatal hippocampal culture (Rohan de Silva et al., 1997). pHluorin was inserted in APP's ectodomain and behind APP's short signaling peptide (SP), ensuring the same subcellular distribution pattern as native APP695 (Bauereiss et al., 2015; Groemer et al., 2011). Intracellular membrane compartments like SVs and endosomes are often acidic (pH 5.5–6.5), whereas extracellular pH is generally neutral (pH 7.35), so pH-APP exhibits increased fluorescence or decreased fluorescence (indicated by bright or dark green circles respectively in Fig. 1A) as APP is externalized or internalized respectively (Groemer et al., 2011).

To independently monitor APP's cytosolic domain, we added a pH-insensitive blue fluorescent protein (BFP2) (Fig. 1A) to pH-APP's C-terminal. Despite the presence of N- and C-terminal pHluorin and BFP2, we expected unaltered APP trafficking and cleavage given previous studies using similar double-labeling strategy (Villegas et al., 2014). To independently detect synaptic boutons and neuronal activity, we added Synaptophysin-pHTomato (Li and Tsien, 2012) and a viral sequence (T2A) in front of the pH-APP-BFP2. By so doing, the SypHTm would be co-transcripted with pH-APP-BFP2 as one piece of mRNA, but translated separately (Osborn et al., 2005). Immunostaining with Synaptotagmin I, an SV-specific protein, confirmed that SypHTm was specific to synapses whereas pH-APP-BFP2 was present across neurites (Supplementary Fig. 1). In live neurons, SypHTm expectedly marked axon terminals, whereas pHluorin and BFP2 neurites are largely overlapped and more diffused in neurons (Fig. 1B).

As described in the Supplementary Results, a series of control experiments were carried out for SypHTm and pH-APP-BFP2. By manipulating intracellular and extracellular pH, we first confirmed that the membrane orientations of SypHTm and pH-APP-BFP2 were correct (i.e. their N-terminal pHTm and pHluorin are located extracellularly and/or luminally). We further confirmed that pH-APP-BFP2 is distributed in the same way as endogenous APP at distal neurites and synapses, and that pH-APP-BFP2 is cleaved by the three major secretases in the same manner as endogenous APP (Supplementary Results). Last but not least, we used whole-cell patch clamp recording to demonstrate that the expression of pH-APP-BFP2 and SypHTm does not alter synaptic transmission.

After validating our reporters, we used live cell imaging to compare APP surface and internal expression in the synaptic and nonsynaptic regions of processes. First, we measured pHluorin or pHTm fluorescence in normal Tyrode's solution (pH 7.3). Next, we applied Tyrode's solution containing 50 mM NH_4Cl to deacidify all intracellular membrane compartments. Finally, we used pH 5.5 Tyrode's to quench all pHluorin or pHTm (Supplementary Movie 1). We calculated (i) the total pHluorin and pHTm (i.e. pH-APP-BFP2 and SypHTm) by subtracting the minimum fluorescence (at pH 5.5) from the maximum fluorescence (at 50 mM NH_4Cl), (ii) the surface (out) pHluorin and pHTm by subtracting the minimum fluorescence (at pH 5.5) from the pretreatment fluorescence (at pH 7.3), and (iii) the intracellular (in) pHluorin and pHTm by subtracting the pretreatment fluorescence (at pH 7.3) from maximum fluorescence (at 50 mM NH_4Cl) (Fig. 1C). At synaptic boutons, we found that the surface pHluorin fraction was significantly higher than the surface pHTm fraction whereas the intracellular pHluorin fraction was significantly lower (Fig. 1D left). At non-synaptic areas, there was little difference between surface and intracellular fractions of pHluorin or pHTm (Fig. 1D right). These observations strongly suggest that, unlike Synaptophysin (Syp), considerable APP present in the surface membranes in addition to SVs, and its apparent enrichment at synaptic boutons may be due to hundreds of clustered SVs there.

2.2. APP and synaptic activity

By imaging pHluorin and BFP2, we asked if APP exhibited activity-associated changes in its subcellular distribution, a question that cannot be readily addressed using conventional biochemical approaches and non-neuronal cells or fixed tissues. We first examined if the intraneurite translocation of APP and/or CTFs was affected by synaptic activity. We applied two discrete stimuli (i.e. a 1-min 10-Hz electric field stimulation and a 1-min 90 mM K^+ perfusion) separated by a 1-min resting period. We monitored the BFP2 signal instead of the pHluorin signal in order to track both surface and intracellular APP, as well as CTF (Fig. 2A and Supplementary Movie 2). Again, SypHTm was used to mark synaptic boutons. The selected BFP2 kymograph exemplifies the diverse trafficking behavior of APP and CTF, i.e. stationary or mobile, anterograde or retrograde, and toward or away from nearby synaptic boutons (Fig. 2B). The SypHTm kymograph was used to show the stationary synaptic boutons. When plotted against time, neither the velocity (Fig. 2C) nor the distance from the nearest synapse (Fig. 2D) of the moving BFP2 puncta exhibited any apparent difference between stimulation and resting periods, suggesting that APP and/or CTFs move along distal neurites rather randomly, at least with respect to the synapses, and are not influenced by neuronal activity.

We then asked if surface-internal turnover of APP is correlated to activity-associated SV exo−/endocytosis at synaptic boutons, which we surveyed by pHluorin and pHTm co-imaging (Fig. 3A). While we did observe an increase of pHluorin fluorescence at synaptic boutons during stimulation (i.e. 90 mM K^+), the amount of increase was not correlated to that of pHTm fluorescence increase (Fig. 3B), suggesting that the magnitude of APP externalization and SV release were discordant. We also compared time courses of fluorescence fluctuations for pHluorin and pHTm during and after the stimulation. Again, they were different,

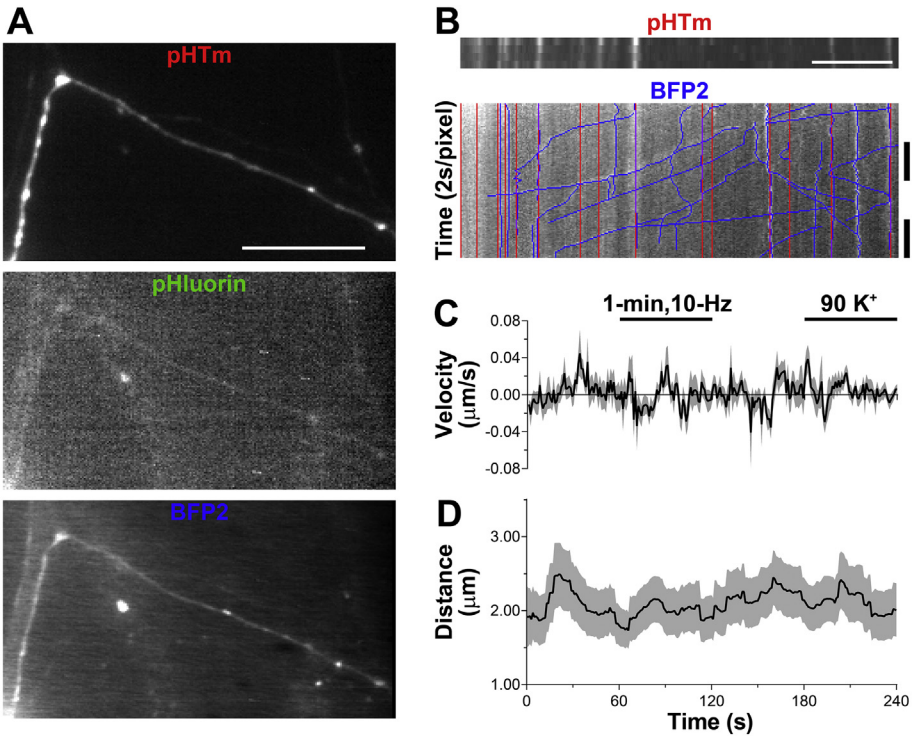

Fig. 2. APP trafficking is not activity-associated. A, sample images of a distal neurite. Scale bar, 10 μm. B, sample kymographs that show the changes in fluorescence over time during 10 Hz field stimulation and 90 K stimulation along the process shown in A. BFP2 was imaged at 0.5 Hz, while pHTm was imaged every minute. Hand drawn BFP2 tracks are shown in blue, stationary synaptic boutons are in red, and purple represents overlap. Scale bar, 10 μm. C, mean velocity of the moving BFP2 puncta. Movement toward the nearest synapse was defined as positive. D, mean distance from the moving BFP2 puncta to the nearest synapse. For C-D, only visible puncta contribute to the mean and SEM, with at most 81 puncta and at least 50 puncta at any given time. In total, 241 tracks are taken from 13 kymographs from 4 trials. Gray shadows represent SEM. (For interpretation of the references to colour in this figure legend, the reader is referred to the web version of this article.)

i.e. the pHluorin fluorescence increase lagged behind that of pHTm (Fig. 3C). Moreover, we did not observe strong correlations for the total, surface, or intracellular pHluorin and pHTm fluorescence intensities (Fig. 3D-F). Together, it is safe to say that APP is not enriched in releasable SVs and its surface turnover is associated but not synchronized with SV turnover.

We also tested if prolonged neuronal activity change alters the synaptic localization and surface-internal trafficking of APP. To do so, we globally enhanced or suppressed neuronal activity by blocking GABAergic (inhibitory) or glutamatergic (excitatory) neurotransmission with 10 μM bicuculline (BCC) or 10 μM 2,3-dihydroxy-6-nitro-7-sulfamoyl-benzoquinoxaline (NBQX) for two hours. Immediately after the treatments, cells were either subjected to live-cell imaging or immunofluorescence staining. In comparison to the sham control (i.e. H_2O), neither BCC nor NBQX treatment changed the surface APP fraction based on the measures of both pH-APP-BFP2 or endogenous APP (Fig. 4A). By contrast, the surface vs. total pHTm ratio and total endogenous Syp significantly increased after NBQX treatment (Fig. 4B), which was expected due to presynaptic homeostasis (Jakawich et al., 2010; Thiagarajan et al., 2005). This again suggests that APP expression or its synaptic localization does not coordinate with neuronal activity. Moreover, ELISA measurements detected no significant difference in Aβ40, Aβ42, or sAPPα extracellular concentration (Fig. 4C-E), which disputes the idea that neuronal activity alters APP cleavage, at least in vitro. Together, our results demonstrate that, other than a limited and delayed coordination between SV and APP turnovers, neuronal activity does not have significant impact on APP surface distribution, trafficking, and cleavage by our measurements.

2.3. Synaptic surface membrane cholesterol and APP distribution

Cholesterol's effects on secretase activities (Bodovitz and Klein, 1996; Grimm et al., 2008; Kojro et al., 2001; Runz et al., 2002; von Arnim et al., 2008; Xiong et al., 2008) and a recently identified cholesterol-binding motif (CBM) within APP (Barrett et al., 2012; Beel et al., 2008; Beel et al., 2010) prompted us to ask if and how a moderate reduction of membrane cholesterol would affect synaptic APP turnover and cleavage. We used a 90-min 1 mM MβCD (methyl-β-cyclodextrin) treatment to reduce cholesterol levels in the synaptic membranes as it did not alter neuron morphology or synaptic transmission (Supplementary Fig. 5A). Measured by Filipin staining, this treatment caused a ~17% reduction of absolute Filipin labeling (47.39 ± 0.34 vs. 39.18 ± 0.60 a.u.) or ~10% (0.6346 ± 0.0064 vs. 0.5686 ± 0.01357 a.u.) after adjusting for membrane density (by AM1–43 co-labeling, please see method section for details) (Supplementary Fig. 5B-D). These relative changes at synaptic boutons may be better quantified by new orthogonal sensors (Liu et al., 2016). Importantly, no apparent membrane damage or morphological change occurred (Supplementary Fig. 5B). Using live cell imaging, we observed that this mild MβCD treatment caused a significant decrease of total pHluorin fluorescence but only an insignificant decrease of BFP2 (Fig. 5A-C), which caused a significant reduction in the total pHluorin vs. BFP2 ratio (Fig. 5D). These results indicate that the mild MβCD treatment led to enhanced α-cleavage of APP in the surface membrane but little change in β/γ-cleavage. Despite the reduction of total APP, MβCD significantly increased the relative fraction of surface APP (Fig. 5E). Similar changes in total and surface pHTm signals were observed, although less significant (Fig. 5F&G).

Since cholesterol modulates the secretases differently and since the secretases cleave APP in different membrane compartments, is it possible that the increase in surface APP fraction was an indirect effect of secretase activity change? We can exclude αS because its upregulation by MβCD should have decreased surface APP fraction. βS is also unlikely because it cleaves intracellular APP and is suppressed by MβCD. Inhibition of γS could increase surface pHluorin and SypHTm fractions in addition to the accumulation of CTF (i.e. increase of BFP2 fluorescence) (Fig. 5B-G). However, the lack of change in BFP2 fluorescence (Fig. 5C) suggests that our mild MβCD treatment was insufficient to affect intracellular γS. Since γS can present in the plasma membrane and form a complex with αS (Chen et al., 2015), is it possible that our MβCD treatment suppressed αS via attached γS? To test this, we applied a γS inhibitor for 24 h. Again, inhibition of γS significantly increased BFP2 fluorescence without altering total pHluorin, leading to a decreased total pHluorin vs. BFP2 ratio (Figs. 5B-D). However, the surface

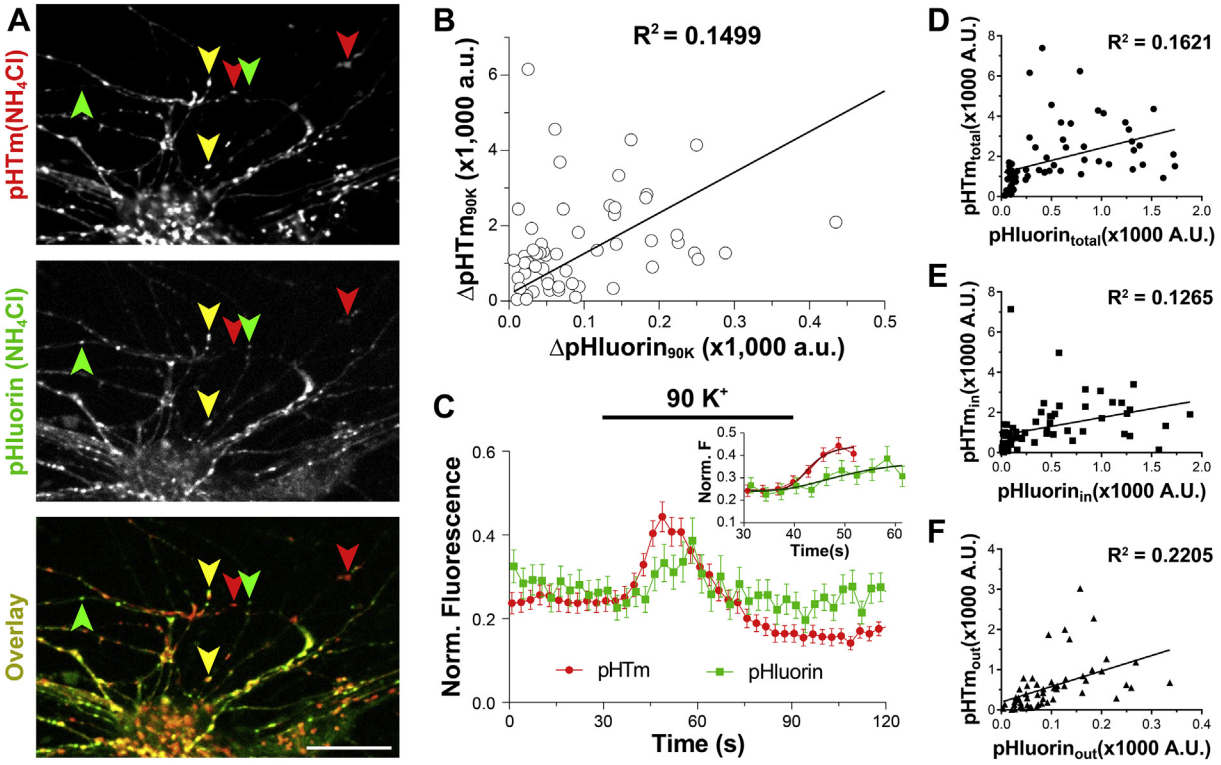

Fig. 3. APP is not highly correlated with acute synaptic activity.
A, sample images of pHTm and pHluorin in NH_4Cl and the overlay. Green arrowheads indicate puncta with high pHluorin and low pHTm fluorescence, red arrowheads indicate the opposite, and yellow arrowheads indicate puncta with similar brightness (i.e. overlapping). Scale bar, 20 μm. B, $\Delta pHTm_{90K}$ and $\Delta pHluorin_{90K}$ represent the maximal increase of fluorescence of every ROI during 90 mM K^+ perfusion. n = 56 ROIs from 3 trials. The line shows a linear regression of slope 1.25 ± 0.36. Pearson's R^2 = 0.1499. C, synaptic pHluorin and pHTm fluorescence normalized to the maximal values set by 50 mM NH_4Cl (mean ± SEM). The pHluorin increase during stimulation with 90 mM K^+ is significantly smaller than that of pHTm according to an unpaired two-tailed t-test (p = .0224). n = 56 ROIs from 3 FOV. The inset shows variable slope (4 parameters) curves fits to the rising phases of pHTm and pHluorin (30 - 60s) with the constraints Top = 0.4437 or Top = 0.3864, which are the maximums of pHTm and pHluorin, respectively. Based on the fittings, for pHTm, $t_{1/2}$ = 12.98 s; for pHluorin, $t_{1/2}$ = 20.15 s. D, total fluorescence ($F_{NH4Cl} - F_{pH5.5}$) of pHTm vs pHluorin. The line shows a linear regression of slope 1.252 ± 0.3585. Pearson's R^2 = 0.1621, p = .0009, n = 65 ROIs from 3 FOVs (excluding negative values). E, internal fluorescence ($F_{NH4Cl} - F_{4K}$) of pHTm vs pHluorin. The line shows a linear regression of slope 0.8808 ± 0.2939. Pearson's R^2 = 0.1265, p = .0039, n = 64 ROIs from 3 FOVs (excluding negative values). F, surface fluorescence ($F_{4K} - F_{pH5.5}$) of pHTm vs pHluorin. The line shows a linear regression of slope 3.86 ± 1.006. Pearson's R^2 = 0.2205, p = .0003, n = 54 ROIs from 3 FOVs (excluding negative values). (For interpretation of the references to colour in this figure legend, the reader is referred to the web version of this article.)

APP increase by γS inhibition, although significant in comparison to DMSO control, is much less than that of MβCD (Fig. 5E), indicating different underlying mechanisms. Moreover, the combination of MβCD and γS inhibitor caused fluorescence changes in pH-APP-BFP2 that were very similar to that caused by MβCD alone (Fig. 5B-E), whereas the changes of SypHTm were different from that of γS inhibitor or MβCD alone (Fig. 5F&G). These results suggest that γS inhibitor and MβCD increase surface APP through different mechanisms and that cholesterol depletion by MβCD treatment is more potent. It is also possible that both γS and cholesterol act on SVs turnover through different mechanisms.

2.4. APP's cholesterol-binding trait affects its surface distribution

To evaluate the physiological relevance of CBM, we introduced two different point mutations (G700A and I703A) into pH-APP-BFP2 separately. Both of them are outside of the major cleavage sites of α/β/γ-S, and are located at or near the APP-cholesterol binding interface according to an NMR study (Barrett et al., 2012). We expressed both wildtype (WT) and mutant forms of SypHTm:T2A:pH-APP-BFP2 in cultured neurons (Fig. 6A). While the expression levels varied, the proteolytic cleavage of all three forms was very similar according to total pHluorin vs. BFP2 ratio (Fig. 6B), suggesting that neither mutation affected secretase cleavage. Intriguingly, both mutations caused a significant increase in the surface fraction of APP (Fig. 6C), suggesting that APP's cholesterol affinity is involved in restricting neuronal surface APP distribution. At the same time, there was no significant increase of surface SypHTm fraction (Fig. 6D), disputing SV's involvement in MβCD-induced change in APP distribution.

Next, we tested if the altered surface distributions of those APP mutants were the result of changes in γ-cleavage, which might be affected by APP's affinity for cholesterol. Again, we used γS inhibitor and observed an increase in BFP2 fluorescence but no significant change in total pHluorin fluorescence (Supplementary Fig. 6), which resulted in a significant decrease of total pHluorin vs. BFP2 ratio in both WT and mutants (Fig. 6E). Thus, neither point mutation interferes with γ-cleavage. While γS inhibition significantly increased the surface APP fraction of WT as we previously observed, it had no effect on either the G700A or I703A mutant (Fig. 6F). There could be two possibilities. One is that those mutations modified the surface APP distribution via a cholesterol-dependent but γS-independent mechanism, and the other is that these mutations simply masked the effect of γS inhibition. The latter is less likely since both mutations are outside of γ-cleavage sites and did not affect γ-cleavage. So, we infer that direct binding of cholesterol to APP either prevents APP from being transported to the surface membrane or promotes its internalization, which is independent of SV turnover or secretase cleavage.

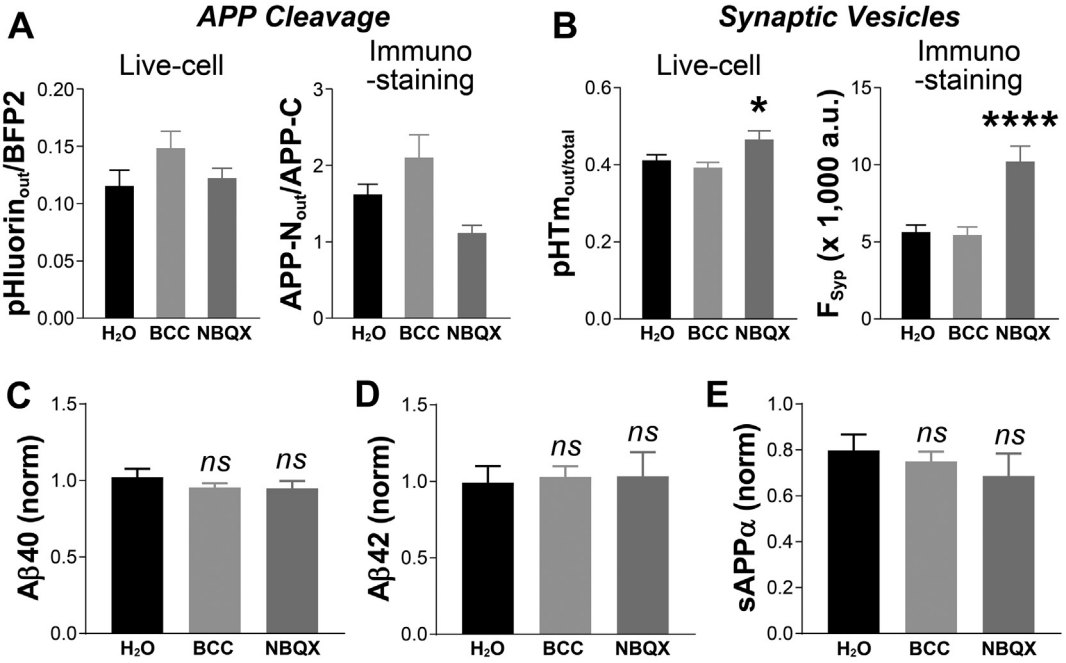

Fig. 4. APP localization and cleavage is not affected by extended increase or decrease of neural network acticity.
A, pHluorin vs. BFP2 ratio (mean ± SEM) after treatment (left) (H_2O = 0.11698 ± 0.0122, BCC = 0.14974 ± 0.0134, NBQX = 0.11565 ± 0.0062). One-way ANOVA detected significant variance in surface pHluorin vs. BFP2 ratio for pH-APP-BFP2 (F (2, 352) = 3.6597, p = .0267). However, Dunnett's multiple comparisons test showed no significant difference between H_2O and bicuculine (BCC) and between H_2O and 2,3-dihydroxy-6-nitro-7-sulfamoyl-benzoquinoxaline (NBQX), (p = .0741 and 0.9941, respectively). n_{H2O} = 80; n_{BCC}, n = 110; n_{NBQX} = 165 synaptic boutons. Surface APP N-terminal vs. total APP C-terminal immunostaining for endogenous APP mean ± SEM (right) (H2O = 1.6416 ± 0.1125, BCC = 2.1239 ± 0.2772, NBQX = 1.1414 ± 0.0749). Although one-way ANOVA detected significant variation in response to treatment (F (2, 447) = 8.2663, p = .0003), Dunnett's multiple comparisons test showed no significant difference between H_2O and BCC and NBQX, (p = .5406 and 0.0117, respectively). All three n = 150 synaptic boutons selected randomly. B, surface vs. total pHTm ratio means ± SEM (left) (H_2O = 0.4628 ± 0.0203, BCC = 0.3866 ± 0.0129, NBQX = 0.4304 ± 0.0159). One-way ANOVA detected significant variance (F (2, 352) = 4.3003, p = .0143), but Dunnett's multiple comparisons test showed no significant difference between H_2O and BCC and significant difference between H_2O and NBQX, (p = .3157 and 0.0084, respectively). Same n as A (left). Immunostaining for endogenous Syp (means ± SEM; right) (H_2O = 5749.1 ± 346.9, BCC = 5566.7 ± 397.4, NBQX = 10,318 ± 901.4). One-way ANOVA detected significant variance (F (2, 447) = 19.9310, p < .0001), but Dunnett's multiple comparisons test showed no significant difference between H_2O and BCC and significant difference between H_2O and NBQX, (p = .8307 and p < .0001, respectively). Same n as A (right). C, ELISA detection of Aβ40, normalized to 0 h vehicle control (H_2O). The means ± SEM are H_2O = 1.0224 ± 0.0547, BCC = 0.9553 ± 0.0281 and NBQX = 0.9491 ± 0.0488. BCC and NBQX treatments do not change Aβ40 levels in the media compared to 2 h treatment with H_2O (One-way ANOVA: F (2, 15) = 0.8034, p = .4662; Dunnett's multiple comparisons test shows that neither treatment causes any significant changes compared with H_2O (BCC, p = .489 and NBQX, p = .4325). D, ELISA detection of Aβ42, normalized to 0 h vehicle control (H_2O). Mean ± SEM: H_2O = 0.9914 ± 0.1092, BCC = 1.0296 ± 0.0696, and NBQX = 1.0342 ± 0.1578. At two hours, Aβ42 level does not vary by treatment (One-way ANOVA, F (2, 15) = 0.0399, p = .9610). Neither treatment causes statistical difference compared to H_2O according to Dunnett's (BCC, ns, p = .9622; NBQX, ns, p = .953). E, ELISA detection of sAPPα after two hours, normalized to 0 h vehicle control (H_2O). The mean ± SEM is H_2O = 0.7979 ± 0.0690, BCC = 0.7502 ± 0.0425, and NBQX = 0.6869 ± 0.0976. Treatment does not cause statistically significant variation according to one-way ANOVA (F (2, 15) = 0.57823, p = .5729) and there is also no significant difference between H_2O and either condition (Dunnett's multiple comparisons test; BCC, p = .8592; NBQX, p = .4738). For C-E, n = 6, where n is three batches of cells and two coverslips per treatment per batch. All error bars represent SEM.

2.5. Binding of cholesterol by APP is important for presynaptic integrity

Since APP regulates membrane cholesterol and since its CBM is involved, we asked whether and how the two APP mutants affect neuronal membrane cholesterol. First, we transfected cells with WT or mutation-bearing SypHTm:T2A:pH-APP; we did not include C-terminal BFP2 because its emission spectrum overlaps with Filipin's. As before, we used AM1–43 co-labeling to normalize the Filipin fluorescence against membrane surface variation. We performed Filipin staining at 4 °C to limit Filipin staining to cell surface membrane (Fig. 7A). To identify transfected neurons and synaptic boutons, we relied on pHTm, which remained fluorescent after fixation. There was significantly less membrane cholesterol in the synaptic boutons of I703A-expressing neurons based on absolute as well as normalized Filipin staining (Fig. 7), and less normalized Filipin in G700A (Fig. 7B2). The effect of those two mutants on membrane cholesterol was dominant-negative as endogenous WT APP was still present in those transfected neurons.

To check membrane cholesterol changes in live neurons, we conducted generalized polarization (GP) imaging (Barrantes et al., 1999). We used C-Laurdan, a derivative of the conventional Laurdan dye. Like Laurdan, it stays in the plasma membrane, absorbs UV excitation (350 nm), and emits blue and green fluorescence. Comparing to Laurdan, it has significantly better photostability and an emission spectrum shift more correlated to membrane cholesterol concentration (Kim et al., 2007). Pixel GP value is calculated as $(F_{blue}\text{-}F_{green})/g$ $(F_{blue} + F_{green})$, in which g is the correction factor. As a ratiometric measure, GP value is insensitive to dye loading variation. We used WT or mutation-bearing SypHTm:T2A:pH-APP (again no BFP2) and different excitations (350 nm for C-Laurdan and 480 for pHluorin) to minize spectral overlap between C-Laurdan and our APP-reporter. As we demonstrated previously (Kitko et al., 2018), GP imaging with C-Laurdan is consistent with Filipin staining in terms of detecting membrane cholesterol change in cultured neurons. Using GP imaging, we visualized the difference in surface membrane cholesterol between WT and APP mutations (Fig. 7C). Again, there were no significant changes in synaptic vesicles between WT and mutant-expressing neurons, indicated by the ratio of out vs. total pHTm (Fig. 7D). But there was significantly less surface membrane cholesterol in the synaptic boutons

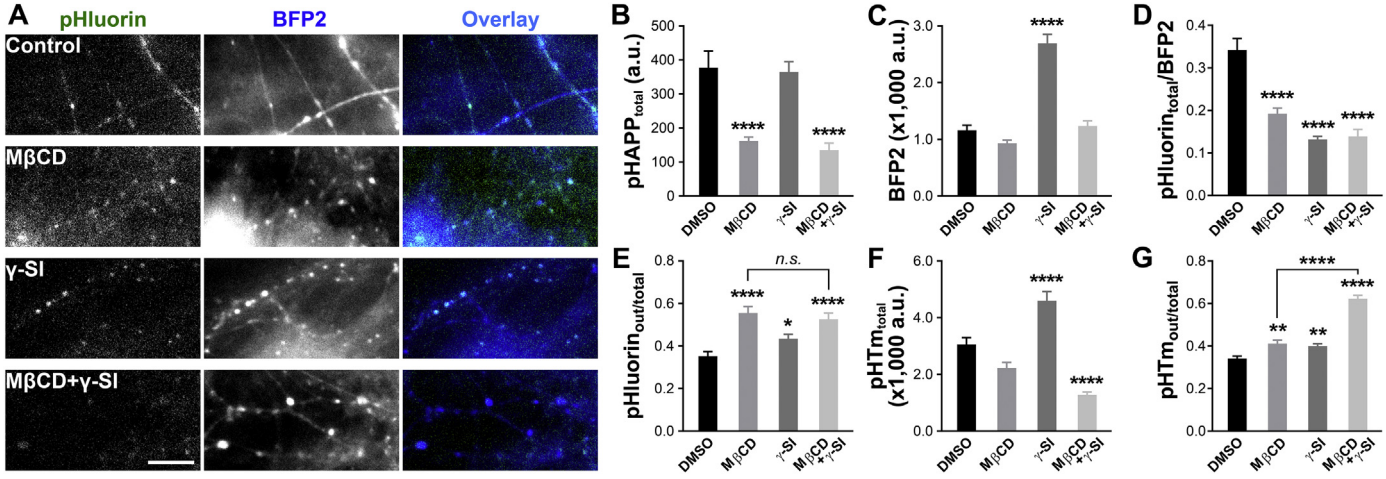

Fig. 5. Membrane cholesterol affects the distribution and cleavage of APP.

A, sample images of pHluorin, BFP2, and their overlays with four different treatments. Scale bar, 10 μm. B, average total pHluorin fluorescence intensities in synaptic boutons marked by SypHTm (mean ± SEM a.u.: DMSO = 377.32 ± 48.97, MβCD = 161.67 ± 11.94, γ-SI = 364.56 ± 30.19, and γ-SI MβCD = 122.54 ± 12.85). One-way ANOVA detected significant differences among treatments ($F(3, 360) = 14.93$, $p < .0001$). Dunnett's multiple comparisons test showed that MβCD significantly decreased total pHluorin fluorescence without or with γ-SI (****, $p = .0001$ for both). However, γ-SI alone made no difference ($p = .9834$). C, average BFP2 fluorescence intensities in synaptic boutons marked by SypHTm (DMSO = 1160.50 ± 88.21, MβCD = 929.84 ± 55.93, γ-SI = 2690.10 ± 161.65, and γ-SI MβCD = 1333.60 ± 112.51). One-way ANOVA detected significant differences among treatments ($F(3, 360) = 48.65$, $p < .0001$). Dunnett's multiple comparisons test showed that only γ-SI significantly increased BFP2 fluorescence compared to WT (****, $p = .0001$). D, average total pHluorin vs. BFP2 ratio in synaptic boutons marked by SypHTm (DMSO = 0.3421 ± 0.0266, MβCD = 0.1922 ± 0.0133, γ-SI = 0.1313 ± 0.0076, and γ-SI MβCD = 0.1323 ± 0.0210). One-way ANOVA detected significant differences among treatments ($F(3, 360) = 35.04$, $p < .0001$). Dunnett's multiple comparisons test showed that MβCD, γ-SI and MβCD + γ-SI significantly decreased the ratio (****, $p = .0001$). E, average surface vs. total pHluorin ratio in synaptic boutons marked by SypHTm (DMSO = 0.3520 ± 0.0217, MβCD = 0.5556 ± 0.0308, γ-SI = 0.4345 ± 0.0206, and γ-SI MβCD = 0.5029 ± 0.0359). One-way ANOVA detected significant differences among treatments ($F(3, 360) = 12.9832$, $p < .0001$). Dunnett's multiple comparisons test showed that both MβCD and γ-SI significantly increased the ratio (****, $p = .0001$; *, $p = .0343$, respectively), as did the combination (****, $p = .0001$), but there is no additive effect for MβCD and γ-SI combined compared to MβCD alone (two-tailed unpaired *t*-test, $p = .4855$). F, average total pHTm in synaptic boutons marked by SypHTm (DMSO = 3058 ± 238, MβCD = 2225 ± 201, γ-SI = 4593 ± 330, and γ-SI MβCD = 1230 ± 122). One-way ANOVA detected significant differences among treatments ($F(3, 360) = 30.86$, $p < .0001$). Dunnett's multiple comparisons test showed that γ-SI significantly increased total pHTm (****, $p = .0001$), whereas MβCD and MβCD + γ-SI decreased it (n.s., $p = .0888$; ****, $p = .0001$, respectively). G, average surface vs. total pHTm in synaptic boutons marked by SypHTm (DMSO = 0.3412 ± 0.0118, MβCD = 0.4119 ± 0.0160, γ-SI = 0.4005 ± 0.0107, and γ-SI MβCD = 0.5878 ± 0.0181). One-way ANOVA detected significant differences among treatments ($F(3, 360) = 76.19$, $p < .0001$). Dunnett's multiple comparisons test showed that MβCD, γ-SI and MβCD + γ-SI significantly increased the ratio (**, $p = .0014$; **, $p = .003$; ****, $p = .0001$, respectively). Additionally, a two-tailed *t*-test showed a significant difference between MβCD + γ-SI and MβCD (****, $p < .0001$). For B-G, $n_{DMSO} = 90$ (FOV = 5); $n_{MβCD} = 75$ (FOV = 5); $n_{γ\text{-}SI} = 119$ (FOV = 7); $n_{MβCD+γ\text{-}SI} = 80$ ROIs (FOV = 4), where n is the number of ROIs corresponding to SypHTm-marked synaptic boutons.

of neurons expressing G700A or I703A (Fig. 7E). So, both Filipin staining and GP imaging results consistently showed that the two mutations reduced cholesterol in the presynaptic plasma membrane.

Given the importance of cholesterol for neuronal membrane integrity (Egawa et al., 2016; Korade and Kenworthy, 2008; Sebastião et al., 2013) and SV turnover (Dason et al., 2014; Pfrieger, 2003), we asked if the two mutations are harmful to synaptic boutons when cells experience the moderate MβCD treatment. In comparison to WT-expressing neurons, we observed significant abnormalities in mutant-expressing boutons after the treatment. In both mutants, we saw severe synaptic deterioration, including swelling, detachment, and failure to respond to NH_4Cl (Fig. 8A). While the ratio of pHTm out vs. total still exhibited a significant increase in response to MβCD in both mutant groups, the magnitude of the increase was less than that of the WT (Fig. 8B, 63% and 38% vs. 83%, two-way ANOVA, $p = .0023$ for the interaction of genotype and treatment). We measured the area of individual pHTm puncta and found significant synaptic swelling in G700A and I703A-expressing neurons after MβCD treatment, with a ~59% and ~38% increase respectively (Fig. 8C). Both mutants made synaptic boutons more vulnerable to mild cholesterol reduction.

To understand how the synaptic deterioration occurred during the MβCD treatment, we performed time-lapse imaging during the treatment and analyzed the fluorescence intensities of pHluorin, BFP2, and pHTm (Fig. 8D-F). During the treatment, synaptic boutons in WT exhibited a mild decrease of pHTm and BFP2 signals and a moderate increase of pHluorin signal, which agreed with previous results (Fig. 5). In the case of G700A, we observed a continuous increase of pHTm and pHluorin signals during the first half of the treatment which was halted in the second half. The BFP2 signal exhibited considerable fluctuation and a very small overall increase. In conjunction with the observed changes in synaptic bouton morphology, we conclude that the increase of pHTm and pHluorin signals likely represents presynaptic swelling and the subsequent cessation of this increase likely reflects presynaptic breakdown. In the case of I703A, there was almost no change in pHTm and BFP2 but a larger and longer increase of pHluorin until the end of the treatment, which is in good agreement with the observed morphological changes and indicates presynaptic swelling but not breakdown. The time-lapse results along with the morphological data suggest that G700A caused a more severe dominant negative effect than I703A did.

3. Discussion

In our study, multi-channel fluorescence imaging and ratiometric analyses enabled a quantitative study of APP distribution in the membranes of intact synaptic boutons of live neurons. These studies took advantage of the unique properties of the triple-fluorescence reporter, SypHTm:T2A:pH-APP-BFP2. Despite being tagged by two fluorescent proteins, pH-APP-BFP2 was distributed and cleaved like endogenous APP. The co-expression of SypHTm not only provided us with a mark for synaptic boutons, but also allowed us to monitor SV turnover. Using both, we were able to evaluate the potential interplay between APP and

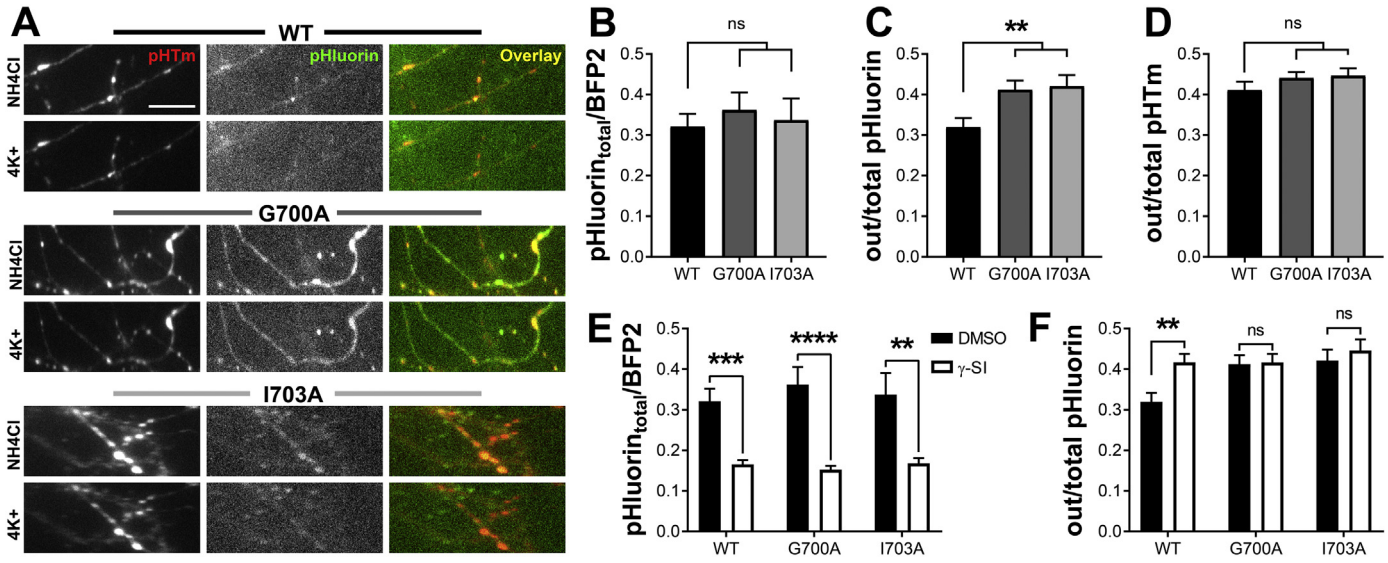

Fig. 6. Point mutations at site located in or close to APP's cholesterol-binding site increase APP surface fraction.
A, sample images of pHTm, pHluorin and their overlays under 50 mM NH_4Cl or 4 K^+ normal Tyrode's solution. Scale bar, 10 μm. B, the average ratio of total pHluorin to BFP2 at the synapses (WT = 0.3213 ± 0.0310, G700A = 0.3623 ± 0.0428, and I703A = 0.3372 ± 0.0530). Neither mutation affects the ratio (one-way ANOVA, F (2, 245) = 0.2601, p = .7712, Dunnett's multiples comparisons test: WT vs. G700A, ns, p = .6976; WT vs. I703A, ns, p = .9539). C, G700A and I703A mutations cause an increase in the surface fraction of pHluorin at the synapses (mean ± SEM, WT = 0.3198 ± 0.0221, G700A = 0.4122 ± 0.0221, and I703A = 0.4211 ± 0.0270; one-way ANOVA, F (2, 245) = 5.652, p = .0040, Dunnett's: WT vs. G700A p = .008; WT vs. I703A p = .0077). D, the pHTm surface fraction is unchanged by the introduction of mutations to pH-APP-BFP2 (mean ± SEM, WT = 0.4114 ± 0.0200, G700A = 0.4416 ± 0.0136, and I703A = 0.4471 ± 0.0172; one-way ANOVA, F (2, 245) = 1.267, p = .2835). E, average pHluorin total to BFP2 ratio shows that both mutants are affected by the γ-SI, demonstrating that γ-secretase is able to cleave them (mean ± SEM, WT = 0.3213 ± 0.0310, G700A = 0.3623 ± 0.0428, I703A = 0.3372 ± 0.0530, WT + γ-SI = 0.1654 ± 0.0105, G700A + γ-SI = 0.1524 ± 0.0096, I703A + γ-SI = 0.1683 ± 0.0129). Two-way ANOVA indicated that only application of the secretase inhibitor affected the pHluorin total to BFP2 ratio. In summary, there was no effect due to mutation (F (2, 531) = 0.1346, p = .8741), significant variance from γ-SI treatment (F (1, 531) = 54.6, p < .0001), and no interaction (F (2, 531) = 0.5277, p = .5903). The results of Sidak's multiple comparisons test comparing only the untreated and the γ-SI treated samples within each APP variant are shown on the plot (WT, ***, p = .0002; G700A, ****, p < .0001; I703A, **, p = .0013). F, interaction between mutations and γ-SI treatment on mean surface fraction of pHluorin at the synapses (mean ± SEM, WT = 0.3198 ± 0.0221, G700A = 0.4122 ± 0.0221, I703A = 0.4211 ± 0.0270, WT + γ-SI = 0.4168 ± 0.0206, G700A + γ-SI = 0.4166 ± 0.0208, I703A + γ-SI = 0.4459 ± 0.0278). Two-way ANOVA was used to investigate the effects of γ-inhibition on the mutants. Although the interaction between APP sequence and γ-SI treatment did not quite reach significance with α = 0.05 (interaction F (2, 531) = 2.421, p = .0898), when Sidak's multiple comparisons test was used only to compare vehicle control to γ-SI, γ-SI significantly increased the pHluorin surface fraction of the wild-type (p = .0062) but not the mutants (G700A, p = .9984 and I703A, p = .8847). ANOVA confirmed that γ-SI treatment (F (1, 531) = 4.791, p = .0290) and cholesterol-binding deficiency (F (2, 531) = 4.022, p = .0185) cause significant alterations in pHluorin surface fraction unlikely to occur by chance when the entire data set is considered. For B–F, n is the total number of synapse ROIs from at least 3 experiments for every condition, and the data set is the same: n_{WT} = 84, n_{G700A} = 96, n_{I703A} = 68, $n_{WT+\gamma\text{-SI}}$ = 112, $n_{G700A+\gamma\text{-SI}}$ = 114 and $n_{I703A+\gamma\text{-SI}}$ = 63. All error bars represent SEM.

SVs and discovered an inverse correlation between synaptic membrane cholesterol and surface APP distribution.

3.1. APP and neuronal activity

It has long been hypothesized that Aβ production/clearance and neuronal activity mutually influence each other and this dysregulation may trigger synaptic dysfunction seen in the initial phase of AD (Musiek and Holtzman, 2015; Selkoe, 2002). Moreover, APP is reportedly enriched in presynaptic terminals (Wilhelm et al., 2014), suggesting a physical coupling between APP trafficking/processing and SV turnover (Fanutza et al., 2015; Groemer et al., 2011; Laßek et al., 2013). Our dual-reporter system (SypHTm and pH-APP-BFP2) allowed us to evaluate the spatiotemporal association between APP and synaptic transmission. While APP is seemingly enriched at synaptic boutons, it is not as exclusive as SV proteins and instead distributes across synaptic and non-synaptic areas. At synaptic boutons, we saw little correlation between full-length APP and Syp on the surface, intracellularly or in total. In addition, neuronal activity did little to synaptic APP distribution or cleavage. Intriguingly, APP did exhibit a delayed surface turnover following strong stimulation (i.e. 2-min, 90 mM K^+). While our data are far from sufficient to dispute the association between APP and neuronal activity, they do suggest an intricate relationship between presynaptic membrane fusion/fission and surface-internal APP turnover. It is worthwhile to better appraise APP distribution in different SV pools and turnover routes by pulse-chase labeling and/or super resolution imaging. Distinguishing full-length APP and its proteolytic products in different presynaptic membranes is also desired, especially given the discrete membrane loci for amyloidogenic and non-amyloidogenic cleavage.

3.2. APP and cholesterol

The inverse correlation between surface APP fraction and membrane cholesterol content independent of cholesterol's impact on secretase activities is another intriguing finding. While cholesterol can shift non-amyloidogenic and amyloidogenic cleavages (Bodovitz and Klein, 1996; Harris et al., 2009; Kim et al., 2016; Kojro et al., 2001; Liu et al., 2009), APP can influence whole-cell cholesterol homeostasis by transcriptional regulation of cholesterol metabolic genes like 3-hydroxy-3-methyl-glutaryl-coenxyme A reductase (Pierrot et al., 2013) and lipoprotein receptor LRP1 (Liu et al., 2007). Our finding adds a new dimension to this mutual relationship, which is more acute and direct. With our moderate MβCD treatment, biochemical measurements for presynaptic surface APP as well as cholesterol would be desired but is currently impractical due to the abundance of astroglia and the limited number of transfected neurons. Nevertheless, two imaging-based tests consistently pointed to decrease in membrane cholesterol and increase

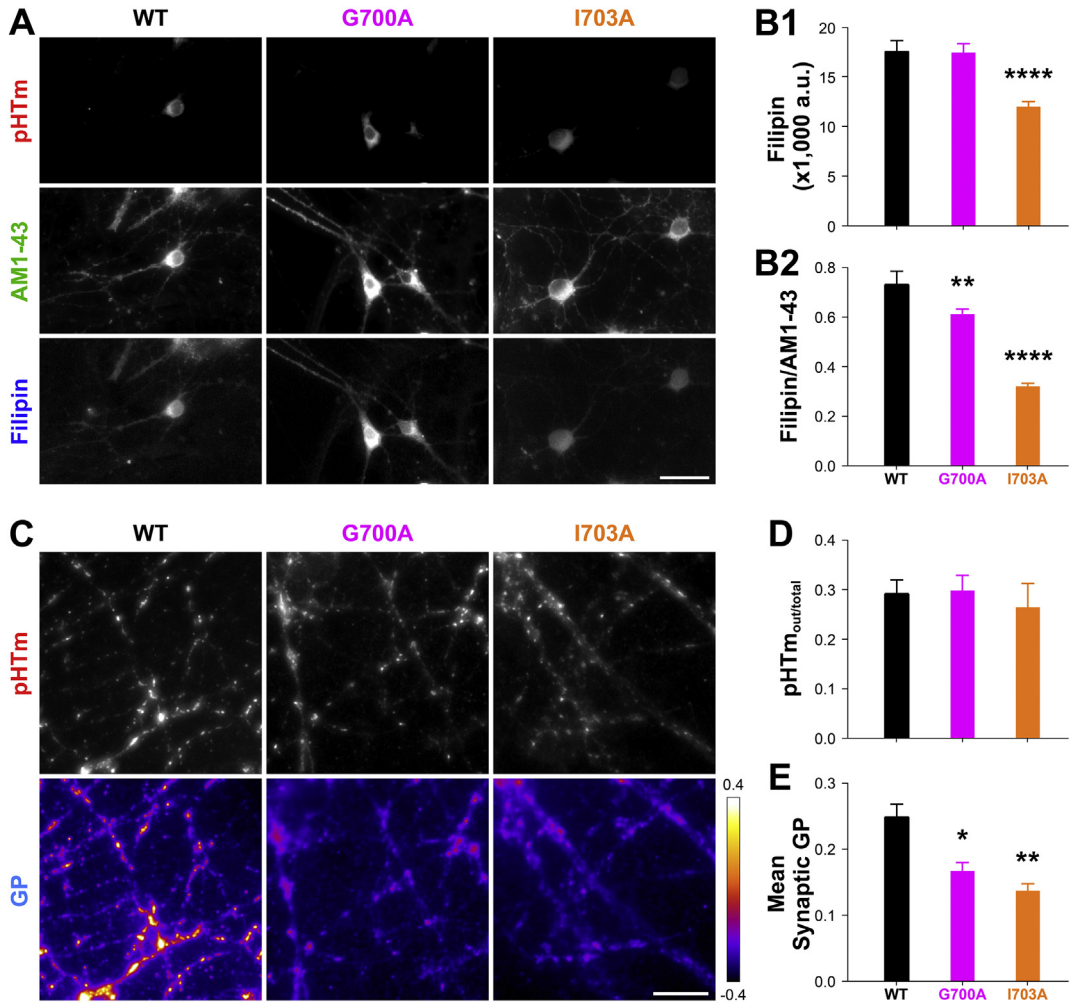

Fig. 7. Point mutations at site located in or near the cholesterol binding site reduce membrane cholesterol at synaptic boutons.
A, sample images of Filipin staining. pHTm fluorescence was preserved after fixation and used to identify transfected neurons. AM1-43 was used to identify neurites and for normalization. Scale bar, 50 µm. B, quantification of Filipin staining. B1, background subtracted filipin signal average ± SEM (17.69 ± 0.95, G700A = 17.57 ± 0.75, I703A = 12.13 ± 0.36, a.u.). One-way ANOVA was used to compare the three conditions and significant variance was detected ($F(2, 911) = 28.349$, $p < .0001$). Cells transfected with I703A have a significantly lower filipin signal compared to WT according to Dunnett's multiple comparisons test (****, $p = .0001$), but there was no difference between G700A and WT (ns, $p = .9908$). B2, mean normalized Filipin signal (Filipin/AM1–43) in transfected process segments, in a.u.: WT = 0.0740 ± 0.0046, G700A = 0.0620 ± 0.0013, I703A = 0.0329 ± 0.0005. Dunnett's multiple comparisons test, performed after one-way ANOVA ($F(2, 911) = 89.127$, $p < .0001$), demonstrates that both G700A (**, $p = .004$) and I703A (****, $p = .0001$) are different from WT. $n_{WT} = 264$, $n_{G700A} = 206$, and $n_{I703A} = 444$, where n is the number of neurite segments from 3 FOVs of each groups. C, top row, sample images of pHTm, which was used to select ROIs corresponding to synaptic boutons. Bottom row, pseudocolored sample GP images of the same FOVs calculated from C-Laurdan's blue and green fluorescence. GP colour scale is from −0.4 to 0.4. Scale bar, 20 µm. D, quantification of surface pHTm fraction (out vs. total). One-way ANOVA was used to compare the three conditions and no significant variance was detected ($F(2, 447) = 0.2799$, $p > .05$). E, mean GP values at ROIs of synaptic boutons of transfected neurons. Dunnett's multiple comparisons test, performed after one-way ANOVA ($F(2, 447) = 9.718$, $p < .0001$), demonstrates that both G700A (*, $p = .03$) and I703A (**, $p = .006$) are different from WT. In D & E, $n = 150$ ROIs randomly selected from 3 FOVs for each group. (For interpretation of the references to colour in this figure legend, the reader is referred to the web version of this article.)

in surface APP fraction at synaptic boutons. Besides secretase, SV exo-/endocytosis (Dason et al., 2010, 2014; Yue and Xu, 2015) can also be excluded as the underlying mechanism because the increase of surface APP did not match that of surface SypHTm. Since point mutations within (Fig. 6) but not outside (data not shown) of its CBM significantly affected APP surface distribution, it is likely that APP's affinity to cholesterol directly facilitate APP internalization or prevent its externalization.

We speculate that APP's acute and direct regulation of membrane cholesterol is particularly important for presynaptic terminals. It is well documented that neurons have more cholesterol (~25%) in their plasma membrane (Wood et al., 2002) than almost any other cells in the body. SVs have an even higher membrane cholesterol concentration (~40%) (Takamori et al., 2006), so massive SV release during neuronal firing imposes a homeostatic challenge at presynaptic terminals. Cholesterol is also essential for SV formation, maintenance (Pfrieger and Barres, 1997), and turnover (Dason et al., 2010, 2014). However, axons often project far from the soma and lack Golgi and endoplasmic reticulum that not only supply cholesterol but also host metabolic regulators like sterol regulatory element binding protein (SREBP) (Ebinu and Yankner, 2002). Therefore, an more immediate regulatory mechanism for presynaptic membrane cholesterol is necessary. APP resembles the SREBP pathway in several aspects including cholesterol-sensitivity, cleavage by regulated intramembrane proteolysis, and the role of their proteolytic products (i.e. transcription factor for cholesterol metabolism genes). Given our observations about APP's redistribution with respect to neuronal activity, γ-secretase inhibition, and MβCD, as well as its affinity to cholesterol, we postulate that APP is a

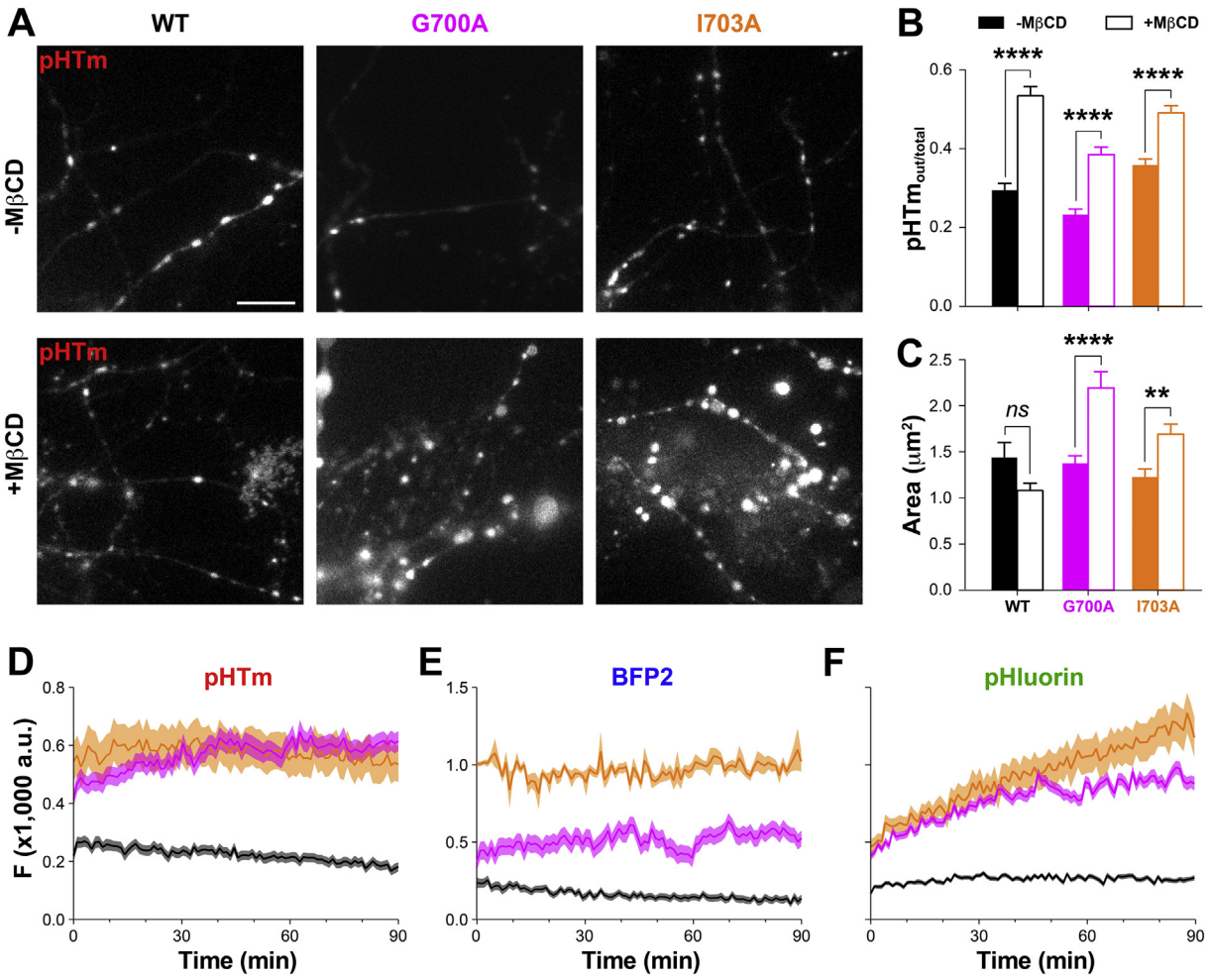

Fig. 8. Point mutations in the cholesterol-binding motif render presynaptic terminals vulnerable to membrane cholesterol reduction.
A, sample pHTm images of transfected neurons with or without MβCD treatment. Cells responded to pH 5.5 but not NH_4Cl were included, because compromised synaptic boutons are intended to be included in this analysis. Scale bar, 10 μm. B, average surface vs. total pHTm ratios of three genotypes with or without MβCD treatment, as mean ± SEM in a.u.: WT = 0.2967 ± 0.0142, G700A = 0.2372 ± 0.0094, I703A = 0.3619 ± 0.0130, WT + MβCD = 0.5389 ± 0.0205, G700A + MβCD = 0.3876 ± 0.0163, and I703A + MβCD = 0.4952 ± 0.0146. Two-way ANOVA detected significant differences between treatments ($F(1, 1131) = 189.1$, $p < .0001$) and genotype ($F(2, 1131) = 38$, $p < .0001$), and there was an interaction ($F(2, 1131) = 6.125$, $p = .0023$). Sidak's multiple comparisons test showed that MβCD had a significant effect on the ratio for all genotypes (WT, ****, $p < .0001$; G700A, ****, $p < .0001$; I703A, ****, $p < .0001$). C, mean area of synaptic boutons ± SEM in μm^2: WT = 1.4719 ± 0.1383, G700A = 1.3912 ± 0.0629, I703A = 1.2441 ± 0.0603, WT + MβCD = 1.0873 ± 0.0629, G700A + MβCD = 2.2139 ± 0.1587, and I703A + MβCD = 1.7108 ± 0.0949. Two-way ANOVA found a significant interaction between the mutation and treatment ($F(2, 1131) = 12.79$, $p < .0001$) and singificant variance based on genotype ($F(2, 1131) = 10.27$, $p < .0001$) and on treatment ($F(1, 1131) = 10.38$, $p = .0013$). Sidak's mutliple comparisons test showed, in fact, that the MβCD's effect on synapse size is specific to the mutants (G700A, ****, $p < .0001$; I703A, **, $p = .0039$) and does not occur in the WT (ns, $p = .1163$). For B&C, $n_{WT} = 131$, $n_{WT+MβCD} = 135$, $n_{G700A} = 182$, $n_{G700A+MβCD} = 235$, $n_{I703A} = 198$, $n_{I703A+MβCD} = 256$, where n is the number of ROIs corresponding to SypHTm-marked synaptic boutons. D-F, average fluorescence changes of pHTm, BFP2 and pHluorin during 90-min 1 mM MβCD treatment. $n_{WT} = 48$ ROIs; $n_{G700A} = 59$ ROIs; $n_{I703A} = 53$ ROIs. Shadows represent SEM.

multifunctional regulator that senses as well as retrieves surface membrane cholesterol and/or balances SV membrane cholesterol (Fig. 9A). This idea also agrees with our observation that APP is in both surface and intracellular membranes at synaptic boutons.

Additionally, both mutants affect membrane cholesterol in a dominant-negative manner. One possible explanation may relate to APP' ability to homo- or heterodimerize with APP and CTF. Indeed, the CBM partially overlaps with the hypothetical APP dimerization motif (Barrett et al., 2012; Yan et al., 2017), and competition between cholesterol-binding and APP/CTF-dimerization has been observed in a biophysical study (Song et al., 2013). Also, APP-CTF heterodimerization may be accountable for the increase of surface APP after γS inhibition (Eggert et al., 2017). Therefore, more studies about APP dimerization and γ-cleavage is also essential. Future investigation about the relationship among neuronal activity, membrane cholesterol and APP trafficking/cleavage is warranted.

3.3. Presynaptic cholesterol and AD

The two APP mutations greatly increased synaptic vulnerability to mild membrane cholesterol reduction, causing significant synaptic swelling and breakdown. It is reminiscent of the synaptic dysfunction and neuronal dysconnectivity preceding neurodegeneration (Musiek and Holtzman, 2015; Selkoe, 2002). This result raises an interesting possibility that the deficiency of presynaptic membrane cholesterol may contribute to AD etiology. Cholesterol has long been suspected as a pathogenic factor for AD. Brain cholesterol is independent of plasma cholesterol, and it is mostly synthetized by astrocytes and supplied to neurons by lipoproteins like ApoE (Wood et al., 2014). In addition to its potential association with amyloid plaque (Liu et al., 2013), ApoE4 is less effective than ApoE2/3 in terms of transporting astrocytic cholesterol to neurons (Mahley, 2016). Age, the primary risk factor for AD, also disrupts brain cholesterol (Wood et al., 2014). Age-related brain

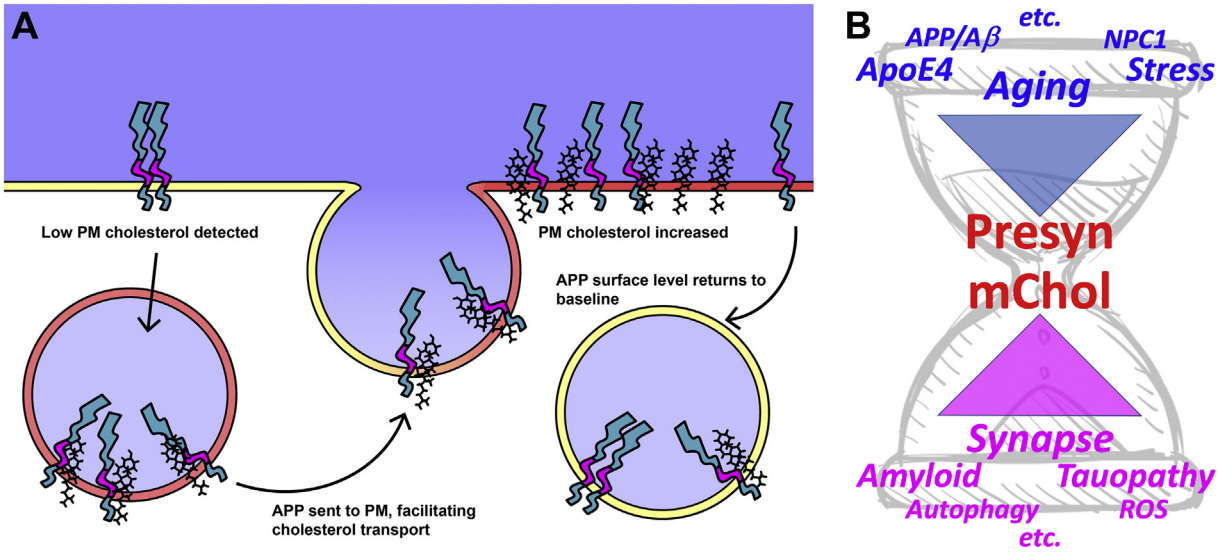

Fig. 9. Schematic models.
A, APP's cholesterol-binding enables translocalization of APP and cholesterol between surface and intracellular membranes at presynaptic terminals. B, various genetic and environmental AD factors converge on presynaptic membrane cholesterol (mChol), and the disruption of presynaptic mChol results in a plethora of pathological changes due to the diverse roles cholesterol play in many cellular pathways. Hourglass represents the aging-dependency of AD.

cholesterol decrease (Martin et al., 2008; Sodero et al., 2011a; Sodero et al., 2011b) is reportedly linked to synaptic dysfunction during the preclinical stage of AD (Abad-Rodriguez et al., 2004; Egawa et al., 2016). Similarly, deficiency in synaptic membrane cholesterol impairs synaptic plasticity, the biological basis of learning and memory (Sebastião et al., 2013). However, others have reported little change or even an increase of cholesterol in synaptosomes isolated from old animals (Eckert et al., 2001; Gibson Wood et al., 2003). Nevertheless, age-related subcellular cholesterol distribution change seems to be more important than global cholesterol change with respect to synaptic function (Peric and Annaert, 2015). Consistently, AD-like histopathologies (e.g. Aβ metabolism, neurofibrillary tangles, and neurodegeneration) occur when intracellular cholesterol transportation to the plasma membrane is disrupted by the NPC1 mutation found in Niemann-Pick Type C1 disease (Malnar et al., 2014; Malnar et al., 2010).

Clearly, presynaptic membrane cholesterol can be disrupted by various genetic as well as environmental factors. Subsequently, many pathophysiological changes can occur because of cholesterol's pleiotropic effects in many neurological processes (Fig. 9B) (Simons and Gerl, 2010; Wood et al., 2011; Wood et al., 2014). In light of our findings, whether presynaptic cholesterol disruption is a more immediate pathogenic factor than APP deserves a more thorough investigation. New tools to monitor and manipulate membrane cholesterol in specific subcellular membranes (Kitko et al., 2018) will be much needed in this regard. Given the increasing capabilities of live-cell imaging, there is now the opportunity to test these hypotheses in brain slices or even in vivo. Indeed, with the help of optogenetics, these ideas can and should be explored in the context of synaptic activity and neuronal network connectivity, which will not only reveal the intrinsic functions of APP but also its etiological relevance to AD.

Supplementary data to this article can be found online at https://doi.org/10.1016/j.nbd.2019.03.009.

Author contributions

C.E. DelBove and Q. Zhang conceived this project, designed experiments, analyzed the data and wrote the manuscript. C.E. DelBove conducted all experiments, with two exceptions. R.M. Lazarenko conducted the electrophysiological experiments. C.E. Strothman conducted SypHTm and pH-APP-BFP2 co-imaging with stimulation by 90 mM K^+. C.E. DelBove, C.R. Sanders and Q. Zhang conceived and designed the APP mutation experiments. H. Huang generated the APP point mutations. We thank X. Deng for experimental help, and all Zhang laboratory members for discussion.

Declaration of interests

All authors declare no competing financial interests.

Acknowledgements

We thank K. E. Kitko for technical help and sharing cell cultures. We thank R.D. Blakely and K.P.M. Currie for comments and discussions. The pHluorin-APP was provided by J. Klingauf lab. We thank all members of the Zhang laboratory for their support. This work is funded by NIH (OD00876101 and NS094738 to Q.Z., and R01 AG056147 to C.R.S.).

References

Abad-Rodriguez, J., Ledesma, M.D., Craessaerts, K., Perga, S., Medina, M., Delacourte, A., Dingwall, C., De Strooper, B., Dotti, C.G., 2004. Neuronal membrane cholesterol loss enhances amyloid peptide generation. J. Cell Biol. 167, 953–960.
Barrantes, F.J., Antollini, S., Massol, R., 1999. Fluorescence studies of the nicotinic acetylcholine receptor in its membrane environment. Biosci. Rep. 19, 335–344.
Barrett, P.J., Song, Y., Van Horn, W.D., Hustedt, E.J., Schafer, J.M., Hadziselimovic, A., Beel, A.J., Sanders, C.R., 2012. The amyloid precursor protein has a flexible transmembrane domain and binds cholesterol. Science 336, 1168–1171.
Bauereiss, A., Welzel, O., Jung, J., Grosse-Holz, S., Lelental, N., Lewczuk, P., Wenzel, E.M., Kornhuber, J., Groemer, T.W., 2015. Surface trafficking of APP and BACE in live cells. Traffic 16, 655–675.
Beel, A.J., Mobley, C.K., Kim, H.J., Tian, F., Hadziselimovic, A., Jap, B., Prestegard, J.H., Sanders, C.R., 2008. Structural studies of the transmembrane C-terminal domain of the amyloid precursor protein (APP): does APP function as a cholesterol sensor?†‡. Biochemistry 47, 9428–9446.
Beel, A.J., Sakakura, M., Barrett, P.J., Sanders, C.R., 2010. Direct binding of cholesterol to the amyloid precursor protein: an important interaction in lipid–Alzheimer's disease relationships? Biochim. Biophys. Acta 1801, 975–982.
Bodovitz, S., Klein, W.L., 1996. Cholesterol modulates alpha-secretase cleavage of amyloid precursor protein. J. Biol. Chem. 271, 4436–4440.
Chen, A.C., Kim, S., Shepardson, N., Patel, S., Hong, S., Selkoe, D.J., 2015. Physical and functional interaction between the alpha- and gamma-secretases: a new model of regulated intramembrane proteolysis. J. Cell Biol. 211, 1157–1176.
Cirrito, J.R., Kang, J.-E., Lee, J., Stewart, F.R., Verges, D.K., Silverio, L.M., Bu, G., Mennerick, S., Holtzman, D.M., 2008. Endocytosis is required for synaptic activity-dependent release of amyloid-beta in vivo. Neuron 58, 42–51.
Das, U., Scott, David A., Ganguly, A., Koo, Edward H., Tang, Y., Roy, S., 2013. Activity-

induced convergence of APP and BACE-1 in acidic microdomains via an endocytosis-dependent pathway. Neuron 79, 447–460.
Das, U., Wang, L., Ganguly, A., Saikia, J.M., Wagner, S.L., Koo, E.H., Roy, S., 2016. Visualizing APP and BACE-1 approximation in neurons yields insight into the amyloidogenic pathway. Nat. Neurosci. 19, 55–64.
Dason, J.S., Smith, A.J., Marin, L., Charlton, M.P., 2010. Vesicular sterols are essential for synaptic vesicle cycling. J. Neurosci. 30, 15856–15865.
Dason, J.S., Smith, A.J., Marin, L., Charlton, M.P., 2014. Cholesterol and F-actin are required for clustering of recycling synaptic vesicle proteins in the presynaptic plasma membrane. J. Physiol. 592, 621–633.
Dawkins, E., Small, D.H., 2014. Insights into the physiological function of the beta-amyloid precursor protein: beyond Alzheimer's disease. J. Neurochem. 129, 756–769.
Ebinu, J.O., Yankner, B.A., 2002. A RIP tide in neuronal signal transduction. Neuron 34, 499–502.
Eckert, G.P., Wood, W.G., Muller, W.E., 2001. Effects of aging and beta-amyloid on the properties of brain synaptic and mitochondrial membranes. J. Neural Transm. 108, 1051–1064.
Egawa, J., Pearn, M.L., Lemkuil, B.P., Patel, P.M., Head, B.P., 2016. Membrane lipid rafts and neurobiology: age-related changes in membrane lipids and loss of neuronal function. J. Physiol. 594, 4565–4579.
Eggert, S., Thomas, C., Kins, S., Hermey, G., 2017. Trafficking in Alzheimer's disease: modulation of APP transport and processing by the transmembrane proteins LRP1, SorLA, SorCS1c, Sortilin, and Calsyntenin. Mol. Neurobiol. 55, 5809–5829.
Fanutza, T., Del Prete, D., Ford, M.J., Castillo, P.E., D'Adamio, L., 2015. APP and APLP2 interact with the synaptic release machinery and facilitate transmitter release at hippocampal synapses. eLife 4.
Gibson Wood, W., Eckert, G.P., Igbavboa, U., Müller, W.E., 2003. Amyloid beta-protein interactions with membranes and cholesterol: causes or casualties of Alzheimer's disease. Biochim. Biophys. Acta 1610, 281–290.
Grimm, M.O.W., Grimm, H.S., Tomic, I., Beyreuther, K., Hartmann, T., Bergmann, C., 2008. Independent inhibition of Alzheimer disease beta- and gamma-secretase cleavage by lowered cholesterol levels. J. Biol. Chem. 283, 11302–11311.
Groemer, T.W., Thiel, C.S., Holt, M., Riedel, D., Hua, Y., Huve, J., Wilhelm, B.G., Klingauf, J., 2011. Amyloid precursor protein is trafficked and secreted via synaptic vesicles. PLoS One 6, e18754.
Haass, C., Koo, E.H., Mellon, A., Hung, A.Y., Selkoe, D.J., 1992. Targeting of cell-surface beta-amyloid precursor protein to lysosomes: alternative processing into amyloid-bearing fragments. Nature 357, 500–503.
Haass, C., Kaether, C., Thinakaran, G., Sisodia, S., 2012. Trafficking and proteolytic processing of APP. Cold Spring Harb. Perspect. Med. 2, a006270.
Hardy, J., Allsop, D., 1991. Amyloid deposition as the central event in the aetiology of Alzheimer's disease. Trends Pharmacol. Sci. 12, 383–388.
Harris, B., Pereira, I., Parkin, E., 2009. Targeting ADAM10 to lipid rafts in neuroblastoma SH-SY5Y cells impairs amyloidogenic processing of the amyloid precursor protein. Brain Res. 1296, 203–215.
Herrup, K., 2015. The case for rejecting the amyloid cascade hypothesis. Nat. Neurosci. 18, 794–799.
Jakawich, S.K., Nasser, H.B., Strong, M.J., McCartney, A.J., Perez, A.S., Rakesh, N., Carruthers, C.J.L., Sutton, M.A., 2010. Local presynaptic activity gates homeostatic changes in presynaptic function driven by dendritic BDNF synthesis. Neuron 68, 1143–1158.
Kang, J., Lemaire, H.G., Unterbeck, A., Salbaum, J.M., Masters, C.L., Grzeschik, K.H., Multhaup, G., Beyreuther, K., Muller-Hill, B., 1987. The precursor of Alzheimer's disease amyloid A4 protein resembles a cell-surface receptor. Nature 325, 733–736.
Kim, H.M., Choo, H.-J., Jung, S.-Y., Ko, Y.-G., Park, W.-H., Jeon, S.-J., Kim, C.H., Joo, T., Cho, B.R., 2007. A two-photon fluorescent probe for lipid raft imaging: C-laurdan. ChemBioChem 8, 553–559.
Kim, Y., Kim, C., Jang, H.Y., Mook-Jung, I., Kim, B., 2016. Inhibition of cholesterol biosynthesis reduces gamma-secretase activity and amyloid-beta generation. J. Alzheimers Dis. 51, 1057–1068.
Kitko, K.E., Hong, T., Lazarenko, R.M., Ying, D., Xu, Y.-Q., Zhang, Q., 2018. Membrane cholesterol mediates the cellular effects of monolayer graphene substrates. Nat. Commun. 9, 796.
Kojro, E., Gimpl, G., Lammich, S., Marz, W., Fahrenholz, F., 2001. Low cholesterol stimulates the nonamyloidogenic pathway by its effect on the alpha -secretase ADAM 10. Proc. Natl. Acad. Sci. U. S. A. 98, 5815–5820.
Korade, Z., Kenworthy, A.K., 2008. Lipid rafts, cholesterol, and the brain. Neuropharmacology 55, 1265–1273.
Kuentzel, S.L., Ali, S.M., Altman, R.A., Greenberg, B.D., Raub, T.J., 1993. The Alzheimer beta-amyloid protein-precursor protease Nexin-ii is cleaved by secretase in a trans-golgi secretory compartment in human neuroglioma cells. Biochem. J. 295, 367–378.
Kügler, S., Meyn, L., Holzmüller, H., Gerhardt, E., Isenmann, S., Schulz, J.B., Bähr, M., 2001. Neuron-specific expression of therapeutic proteins: evaluation of different cellular promoters in recombinant adenoviral vectors. Mol. Cell. Neurosci. 17, 78–96.
Laßek, M., Weingarten, J., Einsfelder, U., Brendel, P., Müller, U., Volknandt, W., 2013. Amyloid precursor proteins are constituents of the presynaptic active zone. J. Neurochem. 127, 48–56.
Li, Y., Tsien, R., 2012. pHTomato, a red, genetically encoded indicator that enables multiplex interrogation of synaptic activity. Nat. Neurosci. 15, 1047–1053.
Liu, Q., Zerbinatti, C.V., Zhang, J., Hoe, H.S., Wang, B., Cole, S.L., Herz, J., Muglia, L., Bu, G., 2007. Amyloid precursor protein regulates brain apolipoprotein E and cholesterol metabolism through lipoprotein receptor LRP1. Neuron 56, 66–78.
Liu, W.W., Todd, S., Coulson, D.T.R., Irvine, G.B., Passmore, A.P., McGuinness, B., McConville, M., Craig, D., Johnston, J.A., 2009. A novel reciprocal and biphasic relationship between membrane cholesterol and beta-secretase activity in SH-SY5Y cells and in human platelets. J. Neurochem. 108, 341–349.
Liu, C.C., Kanekiyo, T., Xu, H., Bu, G., 2013. Apolipoprotein E and Alzheimer disease: risk, mechanisms and therapy. Nat. Rev. Neurol. 9, 106–118.
Liu, S.L., Sheng, R., Jung, J.H., Wang, L., Stec, E., O'Connor, M.J., Song, S., Bikkavilli, R.K., Winn, R.A., Lee, D., et al., 2016. Orthogonal lipid sensors identify transbilayer asymmetry of plasma membrane cholesterol. Nat. Chem. Biol. 13, 268–274.
Mahley, R.W., 2016. Central nervous system lipoproteins: ApoE and regulation of cholesterol metabolism. Arterioscler. Thromb. Vasc. Biol. 36, 1305–1315.
Makin, S., 2018. The amyloid hypothesis on trial. Nature 559, S4–s7.
Malnar, M., Kosicek, M., Mitterreiter, S., Omerbasic, D., Lichtenthaler, S.F., Goate, A., Hecimovic, S., 2010. Niemann-pick type C cells show cholesterol dependent decrease of APP expression at the cell surface and its increased processing through the beta-secretase pathway. Biochim. Biophys. Acta 1802, 682–691.
Malnar, M., Hecimovic, S., Mattsson, N., Zetterberg, H., 2014. Bidirectional links between Alzheimer's disease and Niemann-pick type C disease. Neurobiol. Dis. 72 (Pt A), 37–47.
Martin, M.G., Perga, S., Trovò, L., Rasola, A., Holm, P., Rantamäki, T., Harkany, T., Castrén, E., Chiara, F., Dotti, C.G., et al., 2008. Cholesterol loss enhances TrkB signaling in hippocampal neurons aging in vitro. Mol. Biol. Cell 19, 2101–2112.
Musiek, E.S., Holtzman, D.M., 2015. Three dimensions of the amyloid hypothesis: time, space and 'wingmen'. Nat. Neurosci. 18, 800–806.
Osborn, M.J., Panoskaltsis-Mortari, A., McElmurry, R.T., Bell, S.K., Vignali, D.A.A., Ryan, M.D., Wilber, A.C., McIvor, R.S., Tolar, J., Blazar, B.R., 2005. A picornaviral 2A-like sequence-based tricistronic vector allowing for high-level therapeutic gene expression coupled to a dual-reporter system. Mol. Ther. 12, 569–574.
Parvathy, S., Hussain, I., Karran, E.H., Turner, A.J., Hooper, N.M., 1999. Cleavage of Alzheimer's amyloid precursor protein by alpha-secretase occurs at the surface of neuronal cells. Biochemistry 38, 9728–9734.
Peric, A., Annaert, W., 2015. Early etiology of Alzheimer's disease: tipping the balance toward autophagy or endosomal dysfunction? Acta Neuropathol. 129, 363–381.
Pfrieger, F.W., 2003. Outsourcing in the brain: do neurons depend on cholesterol delivery by astrocytes? BioEssays 25, 72–78.
Pfrieger, F.W., Barres, B.A., 1997. Synaptic efficacy enhanced by glial cells in vitro. Science 277, 1684–1687.
Pierrot, N., Tyteca, D., D'Auria, L., Dewachter, I., Gailly, P., Hendrickx, A., Tasiaux, B., Haylani, L.E., Muls, N., N'Kuli, F., et al., 2013. Amyloid precursor protein controls cholesterol turnover needed for neuronal activity. EMBO Mol. Med. 5, 608–625.
Refolo, L.M., Sambamurti, K., Efthimiopoulos, S., Pappolla, M.A., Robakis, N.K., 1995. Evidence that secretase cleavage of cell surface Alzheimer amyloid precursor occurs after normal endocytic internalization. J. Neurosci. Res. 40, 694–706.
Reinhard, C., Hebert, S.S., De Strooper, B., 2005. The amyloid-beta precursor protein: integrating structure with biological function. EMBO J. 24, 3996–4006.
Rohan de Silva, H.A., Jen, A., Wickenden, C., Jen, L.S., Wilkinson, S.L., Patel, A.J., 1997. Cell-specific expression of beta-amyloid precursor protein isoform mRNAs and proteins in neurons and astrocytes. Brain Res. Mol. Brain Res. 47, 147–156.
Runz, H., Rietdorf, J., Tomic, I., de Bernard, M., Beyreuther, K., Pepperkok, R., Hartmann, T., 2002. Inhibition of intracellular cholesterol transport alters presenilin localization and amyloid precursor protein processing in neuronal cells. J. Neurosci. 22, 1679–1689.
Sebastião, A.M., Colino-Oliveira, M., Assaife-Lopes, N., Dias, R.B., Ribeiro, J.A., 2013. Lipid rafts, synaptic transmission and plasticity: impact in age-related neurodegenerative diseases. Neuropharmacology 64, 97–107.
Selkoe, D.J., 2002. Alzheimer's disease is a synaptic failure. Science 298, 789–791.
Simons, K., Gerl, M.J., 2010. Revitalizing membrane rafts: new tools and insights. Nat. Rev. Mol. Cell Biol. 11, 688.
Sodero, A.O., Trovò, L., Iannilli, F., Van Veldhoven, P., Dotti, C.G., Martin, M.G., 2011a. Regulation of tyrosine kinase B activity by the Cyp46/cholesterol loss pathway in mature hippocampal neurons: relevance for neuronal survival under stress and in aging. J. Neurochem. 116, 747–755.
Sodero, A.O., Weissmann, C., Ledesma, M.D., Dotti, C.G., 2011b. Cellular stress from excitatory neurotransmission contributes to cholesterol loss in hippocampal neurons aging in vitro. Neurobiol. Aging 32, 1043–1053.
Song, Y., Hustedt, E.J., Brandon, S., Sanders, C.R., 2013. Competition between homodimerization and cholesterol binding to the C99 domain of the amyloid precursor protein. Biochemistry 52, 5051–5064.
Sun, J., Roy, S., 2017. The physical approximation of APP and BACE-1 - a key event in Alzheimer's disease pathogenesis. Dev. Neurobiol. 78, 340–347.
Takamori, S., Holt, M., Stenius, K., Lemke, E.A., Gronborg, M., Riedel, D., Urlaub, H., Schenck, S., Brugger, B., Ringler, P., et al., 2006. Molecular anatomy of a trafficking organelle. Cell 127, 831–846.
Thiagarajan, T.C., Lindskog, M., Tsien, R.W., 2005. Adaptation to synaptic inactivity in hippocampal neurons. Neuron 47, 725–737.
van Meer, G., Voelker, D.R., Feigenson, G.W., 2008. Membrane lipids: where they are and how they behave. Nat. Rev. Mol. Cell Biol. 9, 112–124.
Villegas, C., Muresan, V., Ladescu Muresan, Z., 2014. Dual-tagged amyloid-beta precursor protein reveals distinct transport pathways of its N- and C-terminal fragments. Hum. Mol. Genet. 23, 1631–1643.
von Arnim, C.A., von Einem, B., Weber, P., Wagner, M., Schwanzar, D., Spoelgen, R., Strauss, W.L., Schneckenburger, H., 2008. Impact of cholesterol level upon APP and BACE proximity and APP cleavage. Biochem. Biophys. Res. Commun. 370, 207–212.
Wang, H., Megill, A., He, K., Kirkwood, A., Lee, H.-K., 2012. Consequences of inhibiting amyloid precursor protein processing enzymes on synaptic function and plasticity. Neural. Plast. 2012, 1–24.
Wang, Z., Jackson, R.J., Hong, W., Taylor, W.M., Corbett, G.T., Moreno, A., Liu, W., Li, S., Frosch, M.P., Slutsky, I., et al., 2017. Human brain-derived Abeta oligomers bind to synapses and disrupt synaptic activity in a manner that requires APP. Neural Plast. 2012https://doi.org/10.1155/2012/272374. Article ID 272374, (24 pages).

Wilhelm, B.G., Mandad, S., Truckenbrodt, S., Krohnert, K., Schafer, C., Rammner, B., Koo, S.J., Classen, G.A., Krauss, M., Haucke, V., et al., 2014. Composition of isolated synaptic boutons reveals the amounts of vesicle trafficking proteins. Science 344, 1023–1028.

Wood, W.G., Schroeder, F., Igbavboa, U., Avdulov, N.A., Chochina, S.V., 2002. Brain membrane cholesterol domains, aging and amyloid beta-peptides. Neurobiol. Aging 23, 685–694.

Wood, W.G., Igbavboa, U., Muller, W.E., Eckert, G.P., 2011. Cholesterol asymmetry in synaptic plasma membranes. J. Neurochem. 116, 684–689.

Wood, W.G., Li, L., Müller, W.E., Eckert, G.P., 2014. Cholesterol as a causative factor in Alzheimer's disease: a debatable hypothesis. J. Neurochem. 129, 559–572.

Xiong, H., Callaghan, D., Jones, A., Walker, D.G., Lue, L.-F., Beach, T.G., Sue, L.I., Woulfe, J., Xu, H., Stanimirovic, D.B., et al., 2008. Cholesterol retention in Alzheimer's brain is responsible for high beta- and gamma-secretase activities and Aβ production. Neurobiol. Dis. 29, 422–437.

Yan, Y., Xu, T.-H., Harikumar, K.G., Miller, L.J., Melcher, K., Xu, H.E., 2017. Dimerization of the transmembrane domain of amyloid precursor protein is determined by residues around the gamma-secretase cleavage sites. J. Biol. Chem. 292, 15826–15837.

Yue, H.-Y., Xu, J., 2015. Cholesterol regulates multiple forms of vesicle endocytosis at a mammalian central synapse. J. Neurochem. 134, 247–260.